PNAS
www.pnas.org

Main Manuscript for

Mesoscale Bicontinuous Networks in Self-healing Hydrogels Delay Fatigue Fracture

Xueyu Li[a], Kunpeng Cui[b], Tao Lin Sun[a,c,d], Lingpu Meng[e], Chengtao Yu[f], Liangbin Li[e], Costantino Creton[a,g], Takayuki Kurokawa[a,c], and Jian Ping Gong[a,b,c,*]

[a]Global Station for Soft Matter, Global Institution for Collaborative Research and Education (GSS, GI-CoRE), [b]Institute for Chemical Reaction Design and Discovery (WPI-ICReDD), and [c]Faculty of Advanced Life Science, Hokkaido University, Sapporo 001-0021, Japan; [d]South China Advanced Institute for Soft Matter Science and Technology, South China University of Technology, Guangzhou 510640, China; [e]National Synchrotron Radiation Laboratory, Anhui Provincial Engineering Laboratory of Advanced Functional Polymer Film, CAS Key Laboratory of Soft Matter Chemistry, University of Science and Technology of China, Hefei 230026, China; [f]Graduate School of Life Science, Hokkaido University, Sapporo 060-0810, Japan; [g]Laboratoire Sciences et Ingénierie de la Matière Molle, ESPCI Paris, PSL University, Sorbonne Université, CNRS, F-75005 Paris, France

*Jian Ping Gong

Email: gong@sci.hokudai.ac.jp

Costantino Creton ORC ID: 0000-0002-0177-9680

Takayuki Kurokawa ORC ID: 0000-0001-6834-684X

Jian Ping Gong ORC ID: 0000-0003-2228-2750

Classification

Physical Sciences, Applied Physical Sciences

Keywords

fatigue-resistance, hierarchical structure, phase network, crack growth, affine deformation.

Author Contributions

X.L., K.C., T.L.S. and J.P.G. designed the experiments; L.M. and L.L. developed new SAXS measurement set up; X.L., K.C., T.L.S. and C.Y. performed the experiments; X.L., K.C., T.L.S., C.C., T.K. and J.P.G. analysis the data; X.L. and J.P.G. wrote the paper.

This PDF file includes:

Main Text
Figs 1 to 5
Table 1

Abstract

Load-bearing biological tissues, such as muscles, are highly fatigue resistant. Few is understood how the exquisite hierarchical structures of biological tissues contribute to their excellent fatigue resistance. In this work, we study anti-fatigue properties of soft materials with hierarchical structures using polyampholyte hydrogels (PA gels) as a simple model system. PA gels are tough and self-healing, consisted of reversible ionic bonds at the 1 nm scale, crosslinked polymer network at the 10 nm scale, and bicontinuous hard/soft phase networks at the 100 nm scale. We find that the polymer network at the 10 nm scale determines the threshold of energy release rate G_0 above which the crack grows, while the bicontinuous phase networks at the 100 nm scale significantly decelerate the crack advancing until a transition G_{tran} far above G_0. *In-situ* SAXS analysis reveals that the hard phase network suppresses the crack advance to show decelerated fatigue fracture, and G_{tran} corresponds to the rupture of the hard phase network.

Significance

Muscles, composed of exquisite hierarchical structures, exhibit high fatigue-resistance and can resist crack propagation even after injury. The mechanism of the hierarchical structures on suppressing crack advance under reciprocating movement is poorly understood. Tough and self-healing hydrogels are good candidates as simplified model systems for studying the mechanical behaviors of load-bearing bio-tissues. Here, we report that polyampholyte hydrogels, having a hierarchical structure, demonstrate high

fatigue-resistance through a synergistic effect between different scales. Such anti-fatigue mechanism based on hierarchical structure, disclosed for the first time, not only gives important hints to understand fatigue-resistant behavior of bio-tissues with complex hierarchical structures, but also provides design strategy for tough and fatigue-resistant hydrogels by forming multi-scale network structures using non-covalent bonds as building blocks.

Introduction

Suppression and deceleration of crack growth under cyclic loading are observed in load-bearing biological tissues, such as muscles and bones(1, 2). Such anti-fatigue ability of biotissues, which is essential for their functions, should be related to their exquisitely organized hierarchical structures at different scales. For example, skeletal muscles, having a hierarchical structure ranging from folded proteins through non-covalent bonds at molecular scale to muscle fibers at micrometer scale (3, 4), sustain repeated stretching and contraction over 1 billion cycles (5, 6) and crack propagation is suppressed even to an injury (7). On the other hand, common synthetic soft materials are unstructured and usually exhibit poor fatigue resistance as a result of strain concentration at crack tip (8) or polymer network imperfection (9). For example, synthetic hydrogels could be made tough and self-healing by introducing non-covalent bonds to dissipate energy(10, 11), but these tough hydrogels show poor fatigue resistance(12, 13). Above a threshold of energy release rate G_0, the crack grows rapidly with the fatigue cycle. It has been revealed that the threshold G_0 is only determined by the primary network structure of the materials,

which depends on chemical crosslinking density(13-16). The anti-fatigue properties of soft materials are found effectively improved by introducing additional structures to the primary network structure, such as crystals (17-19), composites (20-22) and ordered folded units(23, 24), etc. These results suggest that hierarchical structures may contribute to reduce the strain/stress concentration at the crack tip and hence be beneficial for fatigue resistance in these kinds of soft materials. But the mechanism by which well-designed hierarchical structures at microscopic level can mitigate or suppress crack advance remains poorly understood.

In this work we attempt to elucidate the role of hierarchical structures on the fatigue resistance of self-healing soft materials, focusing on the mechanism of suppression of crack advance and delayed anti-fatigue-fracture. We chose the recently developed self-healing polyampholyte hydrogels (PA gels)(25-27) as model materials. These PA gels, containing ionic bonds at the 1 nm scale, a crosslinked polymer network at the 10 nm scale, and isotropic bicontinuous hard/soft phase networks at the 100 nm scale (**Fig. 1**), exhibit a multiscale response to loads and dissipate large amounts of energy to show a very high toughness (28). Such hierarchical structures make the PA gels good candidates as a simple model system to study the effect of hierarchical structures on the fatigue behavior of self-healing materials containing abundant non-covalent bonds. By combining the fatigue measurement and time-resolved synchrotron radiation small-angle X-ray scattering (SAXS), we discovered that, upon fatigue cycling, the bicontinuous phase networks in PA gels form transient oriented structure to induce a pronounced crack blunting and crack deceleration effect, resulting in an extremely slow mode of crack growth above the energy release rate threshold G_0. This mode is maintained until the

energy release rate exceeds a transition G_{tran} that is several times higher than G_0. Above G_{tran}, the stress-carrying hard phase network ruptures, resulting in an abrupt jump of crack growth to a fast mode. Thus, the 100 nm scale bicontinuous hard/soft phase networks substantially decelerate the fatigue fracture and remarkably enhance the fatigue resistance of the tough hydrogels. Such crack growth decelerating effect by the hierarchical structures in hundred nm scale is observed for the first time in amorphous hydrogels.

Results and Discussion

Tuning Hierarchical Structures in Self-healing Hydrogels

PA gels used in this study were obtained from a chemically crosslinked copolymer consisting of oppositely charged monomers sodium p-styrenesulfonate (NaSS) and methyl chloride quarternised *N*,*N*-dimethylamino ethylacrylate (DMAEA-Q) (*SI Appendix*, **Fig. S1**). The opposite charges on the polymer chains form ionic bonds when the small counter-ions (Na^+ and Cl^-) are removed from the PA gels by dialysis of the samples in pure water. The formation of these ionic bonds induces local aggregation of the polymers, and as a result, the gels form dense hard phase and sparse soft phase inter-connected at ~100 nm scale (28). Such structure acts as bicontinuous hard/soft phase networks. The primary network structure in the 10 nm scale depends on the formulation of monomer and crosslinker concentrations in precursor solution, which controls the crosslinking density of the network from chemical crosslinker and from trapped polymer entanglement, while the contrast and the size of the hard/soft phase networks depend on the primary network structure as well as the temperature at which the dialysis of the PA gels was performed. In this work, we adopted the samples with the same primary network

structure but different phase network structure. For this purpose, the samples were synthesized from the same formulation but dialyzed at different temperatures (see *SI Appendix* for sample preparation). The samples are coded as PA-T_{dial}, where T_{dial} (5 °C, 30 °C and 60 °C) stands for the dialysis temperature. The water content and thickness of these samples were ~46 wt% and ~1.64 mm, respectively, independent of T_{dial}.

First, we show the structure and mechanical behavior of these PA gels. As shown in **Fig. 2*A***, SAXS images of the samples show an isotropic ring and a peak in 1D scattering profiles, attributed to the bicontinuous phase networks consisting of a soft network (with a low modulus) and a hard network (with a high modulus) (28, 29). The intensity of the peak I_m significantly increases with the increase of T_{dial}. Furthermore, the average mesh size of the phase networks, related to the periodicity of the hard and soft phases (d_0), increases slightly with the increase of T_{dial} (**Fig. 2*D***). These results indicate that a higher dialysis temperature induces stronger phase separation, to form bicontinuous networks with a higher density contrast and slightly larger size. Such temperature effect should be attributed to an enhanced hydrophobic interaction of the polymers at high temperature. The tensile behaviors of gels with different phase network structure exhibit little difference (**Fig. 2*B***).

Deformation of Mesoscale Bicontinuous Phase Networks under Tensile

The deformation of the phase networks of PA gels shows three regimes, as observed by *in-situ* time-resolved SAXS during a uniaxial tensile test (*SI Appendix*, **Fig. S3** and **Fig. 2*C*)**. In regime I, the bicontinuous networks deform affinely, assuming incompressibility. That is, the mesh size of the phase networks in the parallel ($d_{//}$) and

perpendicular ($d_{\perp}$) direction obeys $d_{//}/d_0=\lambda$ and $d_{\perp}/d_0=\lambda^{-1/2}$, respectively, with the global elongation ratio λ. As previously demonstrated(28), the loading-unloading curves exhibit a fully recoverable hysteresis in the affine deformation regime. During loading, the ionic bonds break, and the polymer chains in a globule conformation are unfolded, contributing to energy dissipation responsible for toughening the materials; During unloading, the entropic elasticity drives the polymer chains back to their original globule conformation. After a certain waiting time, the temporary ionic bonds formed in the deformed state dissociate and the original ionic bonds in the undeformed state are reformed to show full recovery of structure and properties. In regime II, $d_{\perp}/d_0$ decreases slowly and deviates from affine deformation. In this regime, the first loading sample softens but fully shrinks back to its original size after a sufficiently long waiting time, which indicates that the hard phase network ruptures, while the soft phase network keeps intact providing the entropic restoring force (28). In regime III, $d_{\perp}/d_0$ increases slightly with λ, and the failure of the whole sample occurs soon thereafter, by rupture of the soft phase network. We observe that the maximum stretch ratio for the affine-like deformation of the phase network, λ_{affine}, slightly increases with the dialysis temperature of the samples (**Fig. 2*D***). This order is consistent with the change in the degree of phase contrast and mesh size d_0 of the two networks that both increase with dialysis temperature.

Suppressed Crack Advance and Delayed Fatigue Fracture

Then, we explore the cyclic fatigue behavior in uniaxial tension of these PA samples with differently tuned bicontinuous phase networks. The fatigue experiments were performed using pre-notched samples in the pure shear geometry (insert of **Fig. 3*C***) in a

humidity controlled box (*SI Appendix*, **Fig. S2*A***), following the method by Suo et al.(30). The cyclic fatigue behaviors are found sensitively depended on the relationship between the maximum stretch ratio λ_{max} applied in the cyclic fatigue test and the maximum affine deformation ratio λ_{affine} observed in the tensile test. As shown in **Fig. 3*A*-*C*** for the PA-30 as a representative, we observe a striking difference for λ_{max}=2.94 ($<\lambda_{affine}$) and λ_{max}=3.19 ($>\lambda_{affine}$). For λ_{max}=2.94, a blunt crack tip forms progressively (**Fig. 3*A***). The crack length *c* initially increases fast, but crack growth slows down soon to a much slower crack propagation rate with increasing cycle *N*. The average crack advance rate at steady state $\Delta c/\Delta N$ is extremely small ($\Delta c/\Delta N$=0.028 μm/cycle, red sphere in **Fig. 3*C***). On the other hand, for λ_{max}=3.19, a relatively sharp crack tip is observed (**Fig. 3*B***), and the crack length *c* always increases fast with the number of cycles *N*. The samples failed after only 800 cycles, showing a fast crack propagation rate $\Delta c/\Delta N$ (~59 μm/cycle, red diamond in **Fig. 3*C***), three orders of magnitude larger than that of the sample tested at λ_{max}=2.94.

We observed similar behaviors for PA-5 where the crack length *c* also initially increased fast, slowed down, and finally hardly increased at a representative elongation ratio λ_{max}=2.54 ($<\lambda_{affine}$), while it increased rapidly until fracture of the whole sample at λ_{max}=2.94 ($>\lambda_{affine}$) (*SI Appendix*, **Fig. S4*A***). PA-60 also exhibits the same suppression of crack advance (crack blunting) and fast crack extension behavior at λ_{max}=2.94 ($<\lambda_{affine}$) and λ_{max}=3.84 ($>\lambda_{affine}$), respectively (*SI Appendix*, **Fig. S4*B***).

The λ_{max} dependences of the crack growth rate $\Delta c/\Delta N$ for the three materials with different T_{dial} are shown in **Fig. 3*D***. All the three materials show no measurable crack growth over 40000 cycles below a threshold value of λ_{max} defined here as λ_0. Above λ_0, crack started to grow slowly at steady state. A transition of $\Delta c/\Delta N$ from a slow crack

growth mode to a fast crack growth mode occurred at a value of λ_{max} that we define as λ_{tran}. Specifically, the three materials show a similar threshold value λ_0~2, and the crack advances very slowly ($\Delta c/\Delta N$ < 0.1 μm/cycle) at $\lambda_0 < \lambda_{max} < \lambda_{tran}$, in accompany with crack blunting. At λ_{tran}=2.89±0.07, 3.14±0 and 3.44±0.14 (see *SI Appendix*, **Fig. S5**) for PA-5, 30 and 60, respectvely, a jump of crack growth rate $\Delta c/\Delta N$ to the fast mode ($\Delta c/\Delta N$>10 μm/cycle) occurs (**Fig. 3*D***). The values of λ_{tran} are almost coincident with the values of λ_{affine} observed by the tensile test (**Fig. 2*D***). This result suggests that λ_{tran} corresponds to the limit of affine deformation ratio for the fatigue test, and that the high fatigue resistance is achieved when the hard phase network is intact.

We consider that the coincidence of λ_{tran} and λ_{affine} is due to two reasons. One is that the rupture of the hard phase network occurs at similar elongation ratio λ in fatigue test (in 10 mm × 50 mm pure shear geometry) and in tensile test (in 16 mm × 7.5 mm strip geometry). In fact, the stress-elongation curves of the uniaxial tensile tests in pure shear geometry and in strip geometry almost overlap with each other at small λ that the hard phase network is in the region of affine deformation (*SI Appendix*, **Fig. S6**). Another reason is that there is no strong stress concentration around the crack tip before the rupture of the hard phase network, which is seen in **Fig. 3*A***.

The maximum applied energy release rate G was also calculated from the work of extension of the unnotched sample (9, 30, 31). To obtain a meaningful elastic energy release rate, the hysteresis energy $U_{hys}(\lambda_{max})$ that is dissipated during each cycle by the breaking/reforming of the ionic bonds during loading is excluded from the work of extension, and G was calculated from the equation $G = W_e(\lambda_{max})H_0$, where H_0 is the initial

distance between the two clamps, $W_e(\lambda_{max})$ is the released elastic strain energy density upon unloading for the unnotched sample up to the stretch ratio λ_{max} under the 3000th cycle (at which the sample reached the steady state) (*SI Appendix*, **Fig. S2** ***B*** and ***C***). Even after 3000 cycles the hysteresis loop is still very large (*SI Appendix*, **Fig. S2*D***), indicating that breaking and reforming of the ionic bonds reaches a dynamic equilibrium for that applied deformation rate. Within the range of applied G, two characteristic crack growth modes are observed on a $\Delta c/\Delta N$ versus G plot: a slow crack growth mode with a linear relation $\Delta c/\Delta N=\beta(G-G_0)$ at $G_0<G<G_{tran}$ (**Fig. 3*E***), and a fast crack growth mode after a jump at $G=G_{tran}$ (**Fig. 3*F***), where G_0 is the fatigue threshold, below which the crack does not grow; β is the slope of the linear response region; G_{tran} is the energy release rate at which the crack growth rate transits from slow to fast mode. G_0 and G_{tran} correspond to λ_0 and $\lambda_{tran,}$ respectively. High G_0 and G_{tran}, as well as low β values mean high fatigue resistance. The parameters G_0, β, and G_{tran} extracted from **Fig. 3** ***E*** and ***F*** are summarized in **Table 1**. The β is reduced and G_{tran} is much increased for gels dialyzed at high temperature, consistent with a high value of λ_{affine} and a delay in fatigue fracture. The G_0 for these three samples is almost the same (~68 J/m^2). This is consistent with the reports by Suo et al., showing that the threshold G_0 is determined by the chemically crosslinked polymer network structure (9, 13, 15), which are the same for the three samples. Furthermore, G_0 has the same order of magnitude as the energy required to rupture the polymer strands across the fracture plane, Γ_0, predicted by the Lake-Thomas model(32). The G_{tran} is more than twice higher than G_0 for PA-5, and it increases to about three times and 3.5 times for PA-30 and PA-60, respectively. Since G_{tran} corresponds to

the maximum affine elongation ratio λ_{affine} of the phase networks, the abrupt increase of the crack growth rate at G_{tran} should be related to the breaking of the hard phase network.

The Role of Bicontinuous Phase Networks in Anti-fatigue-fracture

To investigate the effect of the bicontinuous phase networks on the fatigue-resistance behavior, we performed *in-situ* time-resolved SAXS experiments to observe the evolution of the structure of unnotched gels under cyclic tensile deformation with the strip geometry (*SI Appendix*, **Fig. S3*A***). **Fig. 4 *A*** and ***B*** show the stretch ratio of the phase networks in the perpendicular direction $d_\perp/d_0$ versus the maximum applied stretch ratio λ_{max} at the 1st, 3rd, 300th and 1000th cycles, for λ_{max}=2.54 ($<\lambda_{affine}$) and λ_{max}=3.44 ($>\lambda_{affine}$), respectively. The PA-5 sample was adopted as an example. In the case of $\lambda_{max}<\lambda_{affine}$, the $d_\perp/d_0$ always obeys affine deformation from the 1st to the 1000th cycles, except at very small λ (**Fig.4*A***). The latter should be attributed to the residual strain at unloading state. For our consecutive cyclic tensile test at a strain rate (1 s^{-1}), the sample has no enough time to reach full recovery when the sample approaches full unloading (*SI Appendix*, **Fig. S7**). The result suggests that the deformation is reversible under cyclic loading-unloading except for very small λ. This result confirms that the hard network remains intact in cyclic loading. The representative 2D SAXS patterns at different λ for the 1000th cycle are shown in the insert. The scattering intensities exhibit a strongly elongated spot in the perpendicular direction at large deformation (λ=2.54), suggesting the formation of highly anisotropic structure of the phase networks during the cyclic loading. It is also confirmed that no strain-induced crystallization occurs during the cyclic loading. The highly anisotropic hard strands of the intact phase network may carry,

rather homogeneously, most of the stress during loading, as suggested by other oriented hard components in composite materials (17, 20, 21), preventing the stress concentration necessary for crack growth as schemed in **Fig. 4*B***. This is similar to the effect of strain-induced crystallization during fatigue test in elastomers, where the hard crystal reinforces crack tip (19, 33, 34). This explains why crack blunting occurs ahead of the crack tip at $\lambda_{max}<\lambda_{affine}$ during the fatigue test in this work.

On the contrary, when cyclic loads are performed up to $\lambda_{max}>\lambda_{affine}$ (**Fig. 4*C***), $d_{\perp}/d_0$ becomes increasingly larger with increasing number of cycles, deviating from the value predicted by the affine deformation. This suggests that the hard strands gradually rupture with increasing number of fatigue cycles, and the force-carrying ability of the hard strands decreases (*SI Appendix*, **Fig. S8**). Meanwhile, due to the fracture of hard strands during cyclic loading, the recovery and reassociation ability of ionic bonds with their original pairs of the virgin sample decreases, resulting in a decrease of $d_{\perp}/d_0$ at small λ with cycles, as well as a more anisotropic pattern at λ=1 after cyclic loading at λ_{max}=3.44 ($>\lambda_{affine}$) compared with at λ_{max}=2.54 ($<\lambda_{affine}$) (insert in **Fig. 4*C***), and a much smaller hysteresis loop U_{hys} at λ_{max}=3.14 ($>\lambda_{affine}$) than at λ_{max}=2.34 ($<\lambda_{affine}$) (*SI Appendix*, **Fig. S2*D***). Once the hard strands fracture, the soft strands with sparse polymer density may carry most of the load, leading to a fast crack propagation under fatigue test as schemed in **Fig. 4*D***, similar to a single network system(30, 35). That explains why we see a crack velocity jump when the maximum cyclic λ_{max} exceeds λ_{affine} (**Fig. 3*D***).

To further verify the role of the hard strands for the suppression of the fast fatigue crack growth, we turned off the hard strands by preloading the unnotched sample at

$\lambda_{pre}>\lambda_{affine}$, and then performed the fatigue tests immediately at $\lambda_{max}<\lambda_{affine}$ (**Fig. 5*A***). The sample with ruptured hard strands exhibited the fast crack growth mode even at $\lambda_{max}<\lambda_{affine}$ (**Fig. 5*B***). We also preloaded the sample at $\lambda_{pre}<\lambda_{affine}$, a stretch at which the hard strands are not damaged. This preconditioned sample showed even slightly better fatigue resistance than the pristine sample without preconditioning. These results clearly show that the presence of hard strands suppress the fast crack growth in fatigue fracture.

Once the hard strands rupture, the PA gels with intact soft strands act as a single network gel. If we treat the dependence of $\Delta c/\Delta N$ with G in the fast crack propagation regime ($G>G_{tran}$) as a linear relation, the slope β_2 is 3.1×10^{-6}~4.3×10^{-6} $m^3/(J\cdot cycle)$ (*SI Appendix*, **Fig. S9**), close to the β value observed for single networks of PAAm gel (**Table 1**). The slope β_2 slightly increases with dialysis temperature of the samples, which could be associated to the increasing degree of phase contrast of the samples prepared at high dialysis temperature (**Fig. 2*A***). A higher phase contrast indicates a higher concentration contrast and a higher modulus ratio between the hard phase network and the soft phase network. The PA-60, having the relatively weaker soft phase network among the three samples, exhibits the largest exponent β_2. This result indicates that the crack grows faster with a weaker soft phase network when the hard phase network has ruptured. Such mechanism leads to notch sensitivity of the PA gels. The pre-notched sample ruptures at much smaller elongation ratio than the un-notched sample when being compared at the same pure shear geometry, due to rupture of the hard phase network (*SI Appendix*, **Fig. S10**).

Thanks to the role played by hard phase network in PA gels, the fatigue fracture slowed down dramatically above the threshold G_0. The crack advance rate $\Delta c/\Delta N$ is less

than 0.1 μm/cycle and β is as low as 10^{-10} $m^3/(J\cdot cycle)$ below G_{tran}. To see if this fatigue fracture behavior of PA gels is unique to the self-healing PA gels with meso-scale structure, we summarized the reported fatigue fracture behaviors of various hydrogels (9, 12-14, 35) (*SI Appendix*, **Fig. S11**, **Table 1**). We see that the single network PAAm gels and the double network PAMPS/PAAm gels, free of physical bonds, only exhibit a single mode increase of $\Delta c/\Delta N$ above the threshold G_0, although in the double network gels, the crack growth is significantly suppressed, resulting in a very large G_0. On the other hand, the tough and self-healing gels with physical bonds (PAAm-PVA, Ca-alginate/PAAm) also show multi-mode-like fatigue behaviors above the threshold G_0, though not as prominently as the PA gels. Especially, in the case of Ca-alginate/PAAm gels with ionic crosslinks, a relatively clear slow to fast crack growth transition is observed at G_{tran}=84 J/m^2. These results suggest that these gels containing physical bonds may also contain meso-scale structure. In fact, phase separation was observed in PAAm-PVA gels(11, 36). We also see that the β of PA gels and Ca-alginate/PAAm gels with ionic bonds, is orders of magnitude smaller than the PAAm-PVA hydrogels without ionic bonds, which suggests that strong physical bonds play a role to suppress the crack growth in the slow mode regime. These results clearly show that the interplay between different scales of the gels substantially delays the fatigue crack growth.

Conclusion

Most amorphous hydrogels exhibit extremely poor fatigue-resistance. Above the fatigue threshold G_0, which can be predicted by classic Lake-Thomas theory, the fatigue crack grows rapidly to cause sample failure. Thus, the fatigue threshold G_0 has been thought as

the most critical parameter for hydrogels under cyclic loading. In this work, we discovered that the self-healing PA hydrogels with a hierarchical structure exhibit high fatigue resistance due to existence of multi-mode fatigue behaviors. The 10 nm scale polymer network structure determines the fatigue threshold G_0 for the onset of crack growth. While, the phase networks at the 100 nm scale, having ionic bonds at the 1 nm scale as building blocks, decelerate the advancing of fatigue crack dramatically until reaching a transition G_{tran}. Above G_{tran}, which is directly related to the rupture of the hard phase network, fast growth of the fatigue crack occurs. The synergistic effect between the structures at different length scales results in high fatigue resistance. As G_0 and G_{tran} are related to the energy release rates at rupture of the primary network and the hard phase network, respectively, increasing the network density and rupture elongation ratios of these networks at different length scales should enhance the fatigue resistance of the materials. Furthermore, increasing the hierarchy number should induce high order G transitions with large values. The role of hierarchical structures on the delay of fatigue crack advancing elucidated in this work should guide the designing of anti-fatigue soft materials. It also provides clues to understand the fatigue process of biological tissues, which have a more sophisticated hierarchical structure(37-39).

Materials and Methods

Materials. The raw materials cationic monomer methyl chloride quarternised *N,N*-dimethylamino ethylacrylate (DMAEA-Q), anionic monomer sodium p-styrenesulfonate (NaSS), chemical cross-linker N,N-methylenebis(acrylamide) (MBAA), and UV initiator

α-ketoglutaric acid (α-keto) were pursed from Wako Pure Chemical Industries, Ltd (Japan), and used as received.

Preparation of PA gels. Polyampholyte hydrogels (PA gels) were synthesized by a one-step random copolymerization of precursor aqueous solution containing DMAEA-Q, NaSS, MBAA, and α-keto according to previous work (25, 26, 40). The total monomer concentration is C_m=2.0 M, and both of MBAA and α-keto content are 0.1 mol% (relative to C_m).

All details associated with sample preparations, measurement of water content, tensile tests, fatigue tests and SAXS measurements are available in the *SI Appendix*.

Data Availability. All data are included in the main text and *SI Appendix*.

Acknowledgements

This work was supported by JSPS KAKENHI (Grant no. JP17H06144, JP19K23617), and by ImPACT Program of Council for Science, Technology and Innovation (Cabinet Office, Government of Japan). The SAXS experiments were performed at NCPSS BL19U2 beam line at Shanghai Synchrotron Radiation Facility (SSRF), China. Institute for Chemical Reaction Design and Discovery (ICReDD) was established by World Premier International Research Initiative (WPI), MEXT, Japan.

References

1. Taylor D, Hazenberg JG, & Lee TC (2007) Living with cracks: damage and repair in human bone. *Nat. Mater.* 6(4):263.
2. Akkus O & Rimnac CM (2001) Cortical bone tissue resists fatigue fracture by deceleration and arrest of microcrack growth. *J. Biomech.* 34(6):757-764.
3. Edgerton VR, Smith J, & Simpson D (1975) Muscle fibre type populations of human leg muscles. *Histochem J.* 7(3):259-266.
4. Fitts RH (1994) Cellular mechanisms of muscle fatigue. *Physiol. Rev.* 74(1):49-94.
5. Huxley A (1980) *Reflections on muscle* (Liverpool University Press, Princeton, New Jersey).
6. Hunter IW & Lafontaine S (1992) A comparison of muscle with artificial actuators. *Technical Digest IEEE Solid-State Sensor and Actuator Workshop*, (IEEE), pp 178-185.
7. Taylor D, O'Mara N, Ryan E, Takaza M, & Simms C (2012) The fracture toughness of soft tissues. *J. Mech. Behav. Biomed. Mater.* 6:139-147.
8. Mzabi S, Berghezan D, Roux S, Hild F, & Creton C (2011) A critical local energy release rate criterion for fatigue fracture of elastomers. *J. Polym. Sci., Part B: Polym. Phys.* 49(21):1518-1524.
9. Bai R, Yang J, & Suo Z (2019) Fatigue of hydrogels. *Eur J Mech Solid* 74:337-370.
10. Sun J-Y, *et al.* (2012) Highly stretchable and tough hydrogels. *Nature* 489(7414):133.
11. Li J, Suo Z, & Vlassak JJ (2014) Stiff, strong, and tough hydrogels with good chemical stability. *J. Mater. Chem. B* 2(39):6708-6713.
12. Bai R, Yang J, Morelle XP, Yang C, & Suo Z (2018) Fatigue fracture of self-recovery hydrogels. *ACS Macro Lett.* 7(3):312-317.
13. Zhang W, *et al.* (2018) Fracture toughness and fatigue threshold of tough hydrogels. *ACS Macro Lett.* 8(1):17-23.
14. Zhang W, *et al.* (2018) Fatigue of double-network hydrogels. *Eng. Fract. Mech.* 187:74-93.
15. Zhou Y, *et al.* (2020) The Stiffness-Threshold Conflict in Polymer Networks and a Resolution. *Journal of Applied Mechanics* 87(3):031002.
16. Creton C (2017) 50th anniversary perspective: Networks and gels: Soft but dynamic and tough. *Macromolecules* 50(21):8297-8316.
17. Lin S, Liu J, Liu X, & Zhao X (2019) Muscle-like fatigue-resistant hydrogels by mechanical training. *Proc. Natl. Acad. Sci.* 116(21):10244-10249.
18. Lin S, *et al.* (2019) Anti-fatigue-fracture hydrogels. *Sci. Adv.* 5(1):eaau8528.
19. Rublon P, *et al.* (2014) Multiaxial deformation and strain-induced crystallization around a fatigue crack in natural rubber. *Eng. Fract. Mech.* 123:59-69.
20. Li C, Yang H, Suo Z, & Tang J (2020) Fatigue-Resistant elastomers. *J. Mech. Phys. Solids* 134:103751.
21. Xiang C, *et al.* (2019) Stretchable and fatigue-resistant materials. *Mater. Today* https://doi.org/10.1016/j.mattod.2019.08.009.
22. Wang Z, *et al.* (2019) Stretchable materials of high toughness and low hysteresis. *Proc. Natl. Acad. Sci.* 116(13):5967-5972.
23. Kruzic JJ (2009) Predicting Fatigue Failures. *Science* 325(5937):156-158.
24. Suhr J, *et al.* (2007) Fatigue resistance of aligned carbon nanotube arrays under cyclic compression. *Nat. Nanotechnol.* 2(7):417.
25. Sun TL, *et al.* (2013) Physical hydrogels composed of polyampholytes demonstrate high toughness and viscoelasticity. *Nat. Mater.* 12(10):932.
26. Ihsan AB, *et al.* (2016) Self-healing behaviors of tough polyampholyte hydrogels. *Macromolecules* 49(11):4245-4252.
27. Sun TL, *et al.* (2015) Molecular structure of self-healing polyampholyte hydrogels analyzed from tensile behaviors. *Soft matter* 11(48):9355-9366.

28. Cui K, *et al.* (2018) Multiscale energy dissipation mechanism in tough and self-healing hydrogels. *Phys. Rev. Lett.* 121(18):185501.
29. Cui K, *et al.* (2019) Effect of Structure Heterogeneity on Mechanical Performance of Physical Polyampholytes Hydrogels. *Macromolecules* 52(19):7369-7378.
30. Tang J, Li J, Vlassak JJ, & Suo Z (2017) Fatigue fracture of hydrogels. *Extreme Mech. Lett.* 10:24-31.
31. Long R & Hui C-Y (2016) Fracture toughness of hydrogels: measurement and interpretation. *Soft Matter* 12(39):8069-8086.
32. Lake G & Thomas A (1967) The strength of highly elastic materials. *Proc. R. Soc. Lond. A* 300(1460):108-119.
33. Rublon P, *et al.* (2013) In situ synchrotron wide-angle X-ray diffraction investigation of fatigue cracks in natural rubber. *Journal of synchrotron radiation* 20(1):105-109.
34. Mars W & Fatemi A (2002) A literature survey on fatigue analysis approaches for rubber. *Int. J. Fatigue* 24(9):949-961.
35. Zhang E, Bai R, Morelle XP, & Suo Z (2018) Fatigue fracture of nearly elastic hydrogels. *Soft matter* 14(18):3563-3571.
36. Mishra S, Bajpai R, Katare R, & Bajpai AK (2007) On the mechanical strength of biocompatible semi-IPNs of polyvinyl alcohol and polyacrylamide. *Microsystem Technologies* 14(2):193-198.
37. Meyers MA, McKittrick J, & Chen P-Y (2013) Structural biological materials: critical mechanics-materials connections. *Science* 339(6121):773-779.
38. Reznikov N, Bilton M, Lari L, Stevens MM, & Kröger R (2018) Fractal-like hierarchical organization of bone begins at the nanoscale. *Science* 360(6388):eaao2189.
39. Atala A, Kasper FK, & Mikos AG (2012) Engineering complex tissues. *Sci. Transl. Med.* 4(160):160rv112-160rv112.
40. Ihsan AB, *et al.* (2013) A phase diagram of neutral polyampholyte–from solution to tough hydrogel. *J. Mater. Chem. B* 1(36):4555-4562.
41. Bai R, *et al.* (2017) Fatigue fracture of tough hydrogels. *Extreme Mech. Lett.* 15:91-96.

Figures and Table

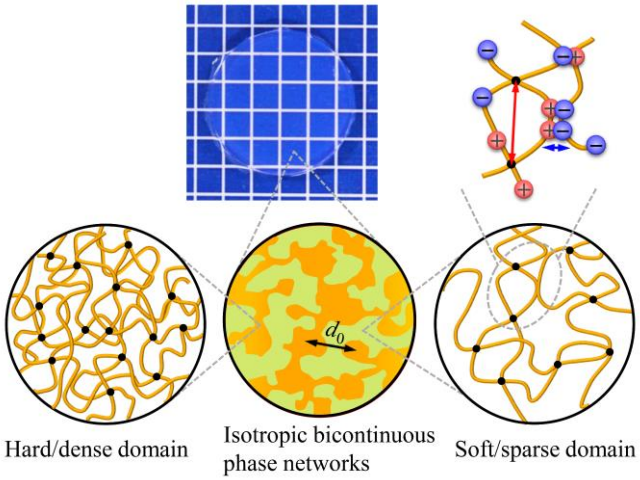

Fig. 1. Illustration for hierarchical structures in PA gels. PA gels are composed of hierarchical structures containing ionic bonds (sacrificial bond) at the 1 nm scale (indicated by blue arrow), crosslinked polymer network with mesh size at the 10 nm scale (indicated by red arrow), and bicontinuous hard/soft phase networks with mesh size at d_0~100 nm scale (indicated by black arrow).

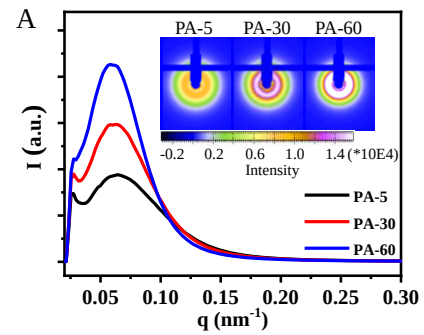

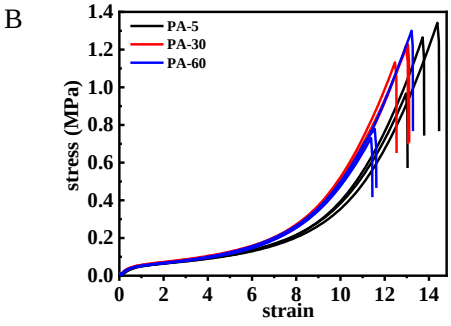

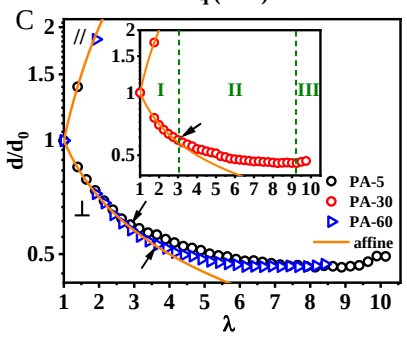

D

Parameters	PA-5	PA-30	PA-60
I_m(a.u.)	9.5±0.8k	14.7±0.3k	21.3±0.5k
d_0 (nm)	95.4±3.4	101.3±4.2	103.8±4.3
λ_{affine}	2.82±0.3	3.06±0.06	3.52±0.18
λ_{tran}	2.89±0.07	3.14±0	3.44±0.14

Fig. 2. Structure and tensile behavior of PA gels used in this study. (***A***) The 1D SAXS profiles of undeformed gels dialyzed at various temperature T_{dial}, coded as PA-T_{dial}. Insert shows the 2D SAXS images. (***B***) Tensile behaviors of the gels. (***C***) Phase network deformation ratio in parallel ($d_{//}/d_0$) and perpendicular ($d_{\perp}/d_0$) directions versus global elongation ratio λ. The orange lines stand for the affine deformation of the phase networks. The maximum affine deformation λ_{affine} for each sample is indicated by arrows. For clarity, the data of PA-30 is shown in insert, and three deformation regimes are marked on it. (***D***) Summary of SAXS peak intensity I_m, average phase network mesh size d_0, maximum affine elongation ratio of phase networks λ_{affine} in tensile test, and critical elongation ratio of fatigue test for fast crack growth, λ_{tran} (extracted from **Fig. 3*D***).

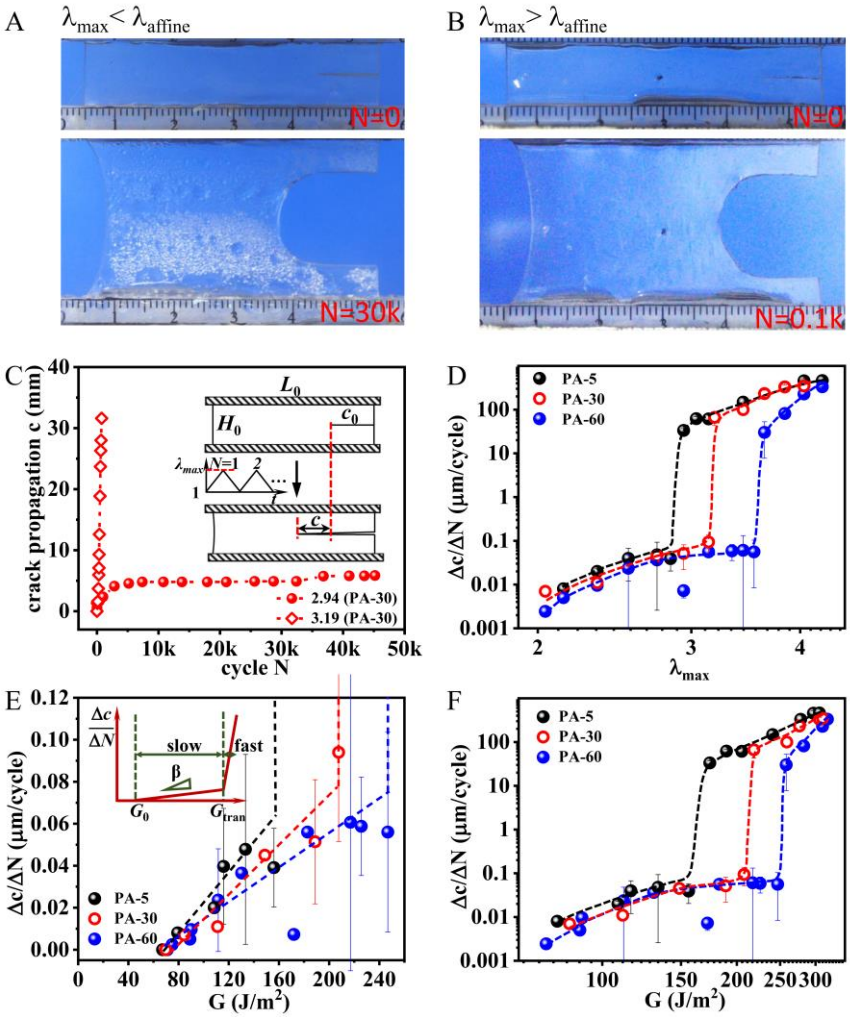

Fig. 3. Delayed fatigue fracture of PA gels. (*A* and *B*) Shape of crack tip for fatigue test under λ_{max}=2.94 ($<\lambda_{affine}$) at 30k cycles (***A***) and λ_{max}=3.19 ($>\lambda_{affine}$) at 0.1k cycles (***B***) for PA-30 as a representative. (***C***) Crack propagation length c as a function of cycle N at elongation ratio λ_{max}=2.94 and 3.19 for PA-30. Insert shows the geometry of sample applied in fatigue test (width L_0 = 50 mm, height H_0 =10 mm, initial notch length c_0=10 mm). (***D***) $\Delta c/\Delta N$ as a function of λ_{max} for gels dialyzed at various temperature T_{dial}. A transition for crack propagation from slow to fast mode is observed universally at λ_{tran}~λ_{affine} for all of the samples. The comparison of λ_{tran} and λ_{affine} is shown in **Fig. 2*D***. (***E***) The enlarged slow mode regime for $\Delta c/\Delta N$ as a function of energy release rate G. A linear relation $\Delta c/\Delta N=\beta(G-G_0)$ at $G_0<G<G_{tran}$, is observed (as schemed in insert). The G_0, β, and G_{tran} are shown in **Table 1**. (***F***) The $\Delta c/\Delta N$ as functions of G in log-log plot. $\Delta c/\Delta N$ jumps from a low plateau (<0.1 μm/cycle) to a high value (>10 μm/cycle) at $G=G_{tran}$. The dashed lines are guide for the eyes. The average crack advance velocity $\Delta c/\Delta N$ is estimated from the slope at steady state. The $\Delta c/\Delta N$ values at the boundary of the transition regime in ***D***, ***E***, ***F*** are obtained from the statistical average values of the high probability mode at the corresponding λ_{max} (see *SI Appendix*, **Fig. S5**).

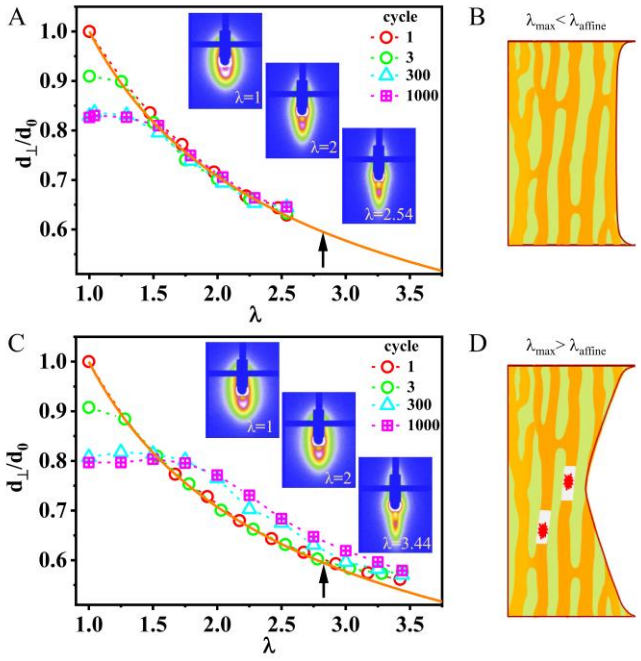

Fig. 4. Structure evolution of PA gels under cyclic tensile deformation. (***A*** and ***C***) Microscopic deformation under cyclic loading at λ_{max}=2.54 ($<\lambda_{affine}$) (***A***) and λ_{max}=3.44 ($>\lambda_{affine}$) (***C***) for unnotched PA-5 gel. Insert shows the SAXS patterns (the stretching is along horizontal direction) at representative λ under the 1000th cycle. The orange solid line in each figure is for affine deformation. The dashed lines are guide for the eyes. The black arrow in each figure is the maximum λ to show affine deformation λ_{affine}. (***B*** and ***D***) Illustration of bicontinuous phase network deformation and rupture at λ_{max} of fatigue test for $\lambda_{max}<\lambda_{affine}$ (***B***) and $\lambda_{max}>\lambda_{affine}$ (***D***), respectively.

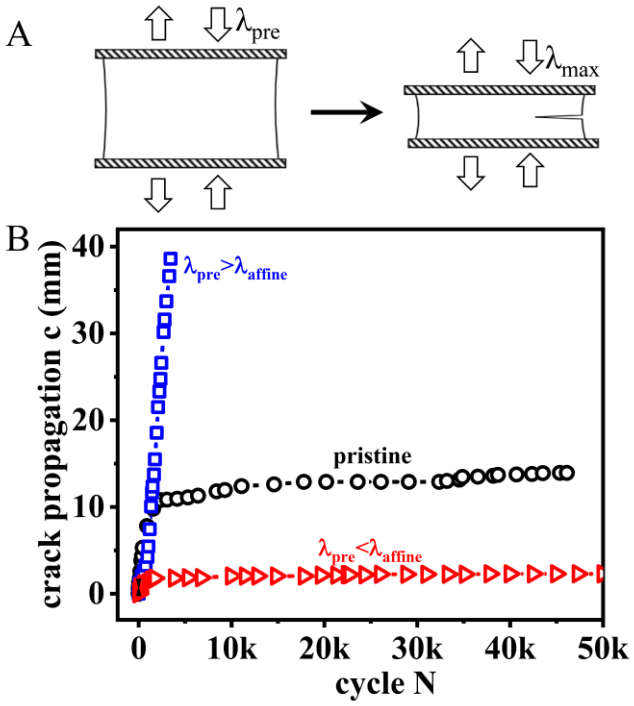

Fig. 5. Turning off hard phase network and its effect on fatigue behavior. (***A***) The experimental protocol to turn off hard phase network: the unnotched PA-5 sample is firstly preloaded at λ_{pre}=3.44 (>λ_{affine}) for 1000 cycles, then a notch is made and fatigue test is performed at λ_{max}=2.54 (<λ_{affine}). For comparison, sample with λ_{pre}=2.74 (<λ_{affine}) is also studied. (***B***) Fatigue experimental results for samples experienced different preloading. (blue) λ_{pre}=3.44 (>λ_{affine}) with ruptured hard phase network; (red) λ_{pre}=2.74 (<λ_{affine}) with undamaged hard phase network; (black) pristine sample without preloading.

Table 1. Comparison of fatigue parameters of PA gels with various hydrogels.

Sample	E^a (MPa)	G_0 (λ_0) (J/m^2)	β ($m^3/(J\cdot cycle)$)	G_{tran} (J/m^2)
PA-60	0.14	71.1 (1.94)	4.1×10^{-10}	236.2±15.0
PA-30	0.14	69.8 (1.94)	6.1×10^{-10}	207.6±0
PA-5	0.14	67.3 (2.04)	7.3×10^{-10}	165±12.7
Alginate/ PAAm (13, 41)	~0.1	35 (1.9)	$(1.3\sim2.3)\times10^{-9}$	84
PAAm-PVA(12)	~0.03	9.5 (1.4)	5.3×10^{-7}	40
PAMPS/PAAm DN (14)	~0.3	200~418 (~1.5)	$(1.3\sim4.5)\times10^{-9}$	--
PAAm (30, 35)	~0.04	4.3~64.5 (~1.3)	$(0.3\sim3.4)\times10^{-7}$	--

[a]The Young's modulus *E* is tested under the same condition for fatigue test.

PNAS
www.pnas.org

Supplementary Information for

Mesoscale Bicontinuous Networks in Self-healing Hydrogels Delay Fatigue Fracture

Xueyu Li, Kunpeng Cui, Tao Lin Sun, Lingpu Meng, Chengtao Yu, Liangbin Li, Costantino Creton, Takayuki Kurokawa, and Jian Ping Gong*

*Jian Ping Gong

Email: gong@sci.hokudai.ac.jp

This PDF file includes:

Supplementary Information Text

Methods

Preparation of polyampholyte hydrogels (PA gels). Polyampholyte hydrogels (PA gels) were synthesized by a one-step random copolymerization of precursor aqueous solution containing anionic monomer sodium p-styrenesulfonate (NaSS), cationic monomer methyl chloride quarternised *N*,*N*-dimethylamino ethylacrylate (DMAEA-Q), UV initiator α-ketoglutaric acid, and chemical cross-linker N,N-methylenebis(acrylamide) (MBAA) (the structures are presented in **Fig. S1**) according to refs (1-3). The total monomer concentration C_m is 2.0 M with monomer ratio of NaSS:DMAEA-Q=0.515:0.485, and both of the UV initiator and cross-linker content are 0.1 mol% (relative to C_m) in the precursor solution. The precursor solution was degassed and then injected into a reaction cell (20 cm×20 cm) consisting of a pair of parallel glass plates separated by a silicone spacer with thickness of 2 mm in argon atmosphere. Polymerization was carried out in argon atmosphere keeping the oxygen concentration less than 0.1 ppm by irradiating UV light (wavelength 365 nm, light intensity ~4mWcm^{-2}) from both sides of the reaction cell for 11 h. After polymerization, the as-prepared gels were taken out and immersed in de-ionized water to dialyze the counter-ions and to reach equilibrium. To tune the bicontinuous hard/soft phase networks, the as prepared gels in the same batch were dialyzed in water with temperature T_{dial}=5, 30 and 60 ℃, respectively. The dialyzed samples contain no small counter-ions. After dialysis, gels were stored at room temperature before use. The gels shrink to ~1.64 mm in thickness after dialysis, denoted as PA-T_{dial}.

Water content. The water content of the gels c_w (wt%) was measured using the moisture balance (Moisture Balance; MOC-120H, Shimadzu Co.), where the weight change of samples was monitored during the drying process. The c_w are 0.461±0.41, 0.455±0.13 and 0.455±0.23 for PA-5, PA-30 and PA-60, respectively.

Tensile tests. The tensile tests were carried out on dumbbell shaped samples with the standard JIS-K6251-7 size 12 mm in gauge length (L_0) × 2 mm in width (w_0) using an INSTRON 5566 universal tensile tester. To prevent water from evaporating from the samples, the dialyzed sample were tested under constant moisture environment. A constant velocity v=10 mm/s was applied during the stretching. The nominal stress was obtained from the tensile force divided by the initial cross-sectional area of the sample and the elongation ratio λ was obtained from the ratio of the stretching length L and the initial length L_0.

Fatigue experiments. Fatigue experiments were performed on a tensile tester (Shimadzu Autograph AG-X tensile machine) with a 100 N load cell. Two different samples with pure shear geometry (10×50×1.64 mm^3, H_0×L_0×t), single-edge notched and unnotched, were used. To prevent samples from dehydrating, a humidity chamber was set on the tensile tester. Water vapor was sustainably supplied in the chamber during the test (**Fig. S2*A***). Cyclic loading-unloading was performed along the H_0 direction at a nominal strain rate of 1 s^{-1} with the maximum elongation ratio in each cycle held at λ_{max}, while the minimum held at λ=1. The test temperature was kept constant at 24 ℃. A digital camera (canon 7D) was used to record photos during crack extension for notched samples every 5 min. The resolution of this optical method is 10 μm. The length of crack extension during cyclic loads was recorded as c. To improve the reliability of results, fatigue tests

were performed at least twice for several representative values of λ_{max}. The amplitude of load in terms of the energy release rate G was calculated from

$$G = W_e(\lambda_{max})H_0 \qquad \text{(S1)}$$

where H_0 is the initial distance between the two clamps, $W_e(\lambda_{max})$ is the elastic strain energy density of the unnotched sample at steady state. Softening and shakedown were observed during cyclic loading for unnotched sample. After 3000 cycles, the cycle approaches steady state (**Fig. S2 *B* and *C***). At steady state, gels still exhibit a large hysteresis loop, caused by the fast dissociation and reassociation of weak ionic bonds (**Fig. S2*D***), which contribute to the nominal fracture energy Γ. Here, to obtain the intrinsic fracture energy, the hysteresis energy was excluded. Thus, the integral area under the unloading curve $W_e(\lambda_{max})$ at the 3000th cycle was used to calculate G.

The fatigue threshold predicted by Lake-Thomas model(4, 5) $\Gamma_0 = \Sigma U_{c\text{-}c} N_e$ is ~24 J/m^2 for the PA gels with different T_{dial} applied in this work, where, Σ is areal density of chains crossing the interface (~2.24×10^{16} /m^2), $U_{c\text{-}c}$ is the energy stored per C-C bond (347 kJ mol^{-1}), N_e is the average number of bonds per polymer strand (~2000 bonds between two crosslinks)

In-situ SAXS measurements during stretching. The evolution of bicontinuous phase structure in PA gels during stretching was characterized by *in-situ* small-angle X-ray scattering (SAXS), which was carried out at the Shanghai Synchrotron Radiation Facility (BL19U2, Shanghai, China). The X-ray wavelength is 1.03 Å. A two-dimensional detector (Pilatus 1M with a resolution of 981×1043 pixels and pixel size of 172 μm,

Dectris Co. Ltd) was used to record data. The sample-to-detector distance was 5730 mm. A tensile machine with well controlled humidity and temperature (Hefei Puliang Technology Co., Ltd) was used to perform uniaxial tensile and cyclic loading experiments. The nominal loading strain rate was controlled to be 1 s^{-1}. Experimental temperature is 24 ℃. 2D SAXS patterns were acquired at a rate of 0.25 s/frame. The resulting strain, stress and SAXS patterns were recorded.

The *in-situ* SAXS experiments were performed on samples with a tensile strip geometry. As the bicontinuous phase networks of PA gels has a large phase mesh size d_0, the scattering signal parallel to deformation direction exceeds the detecting range at large λ_{max}. To obtain the microscopic structural information under stretch, the signal from the direction perpendicular to the stretch direction had to be used. For a pure shear geometry(6, 7), the affine deformation follows $\lambda_1=\lambda$(parallel to stretching direction), $\lambda_2=1$ (sample width direction), $\lambda_3=1/\lambda$ (sample thickness direction), since the gels are incompressible. Therefore, no deformation occurs in the width direction perpendicular to the stretching. Furthermore, SAXS could not measure the structural change in the thickness direction to obtain λ_3. Thus, instead of pure shear geometry, we used gels with a strip geometry (16×7.5×1.64 mm^3, **Fig. S3*A***), which should follow $\lambda_1=\lambda$, $\lambda_2=\lambda_3=1/\sqrt{\lambda}$ for affine deformation. The deformation of the phase mesh size $d_\perp$ in the perpendicular direction was detected until the fracture of the sample (**Fig. S3 *C* and *E***).

The evolution of SAXS patterns during tensile test for the representative gels PA-5 and PA-60 are presented in **Fig. S3*C***. The initial scattering intensity of PA-60 is much stronger than that of PA-5, indicating a stronger phase contrast. The undeformed gels show an isotropic ring on the 2D SAXS pattern. It converts into an ellipse with its major

axis being perpendicular to the stretching direction with increasing λ, suggesting an elongation of the phase structures in the stretching direction. The scattering signal in the stretching direction gradually moves toward the beam stop with increasing λ and exceeds the detectable range after λ=1.8, while the signal in the perpendicular direction moves away from the beam center with increasing λ, and finally converts to two slender intense spots (**Fig. S3*C***). These results indicate the formation of highly oriented structure along the stretching direction.

To investigate the effect of the bicontinuous phase networks on the fatigue-resistance behavior, *in-situ* time-resolved SAXS experiments were performed to observe the evolution of the structure under cyclic tensile deformation using samples with geometry in **Fig.S3*A*.** PA-5 was chosen as a representative. Samples are subjected to cyclic loading for 1000 cycles at λ_{max}=2.54 ($<\lambda_{affine}$) and λ_{max}=3.44 ($>\lambda_{affine}$) under nominal loading strain rate 1 s^{-1}. The SAXS data were collected at the 1st, 3rd, 300th and 1000th cycles.

Fit 2D software from the European Synchrotron Radiation Facility was used to analyze SAXS data. The background scattering from the air and water was subtracted from the data. The 2D SAXS patterns were integrated along the azimuthal direction to obtain 1D scattering profiles as a function of the scattering vector

$$q = 4\pi\left(sin\ \theta\right)/\ \lambda \qquad \text{(S2)}$$

where q is the module of scattering vector, 2θ the scattering angle, and λ the X-ray wavelength. The spacing between adjacent hard (soft) phases (phase network mesh size, d) was obtained from the position of the scattering maxima q_{max} according to Bragg's law

$$d = 2\pi / q_{max} \qquad \text{(S3)}$$

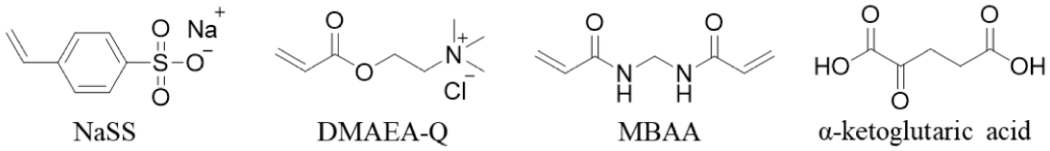

Fig. S1.

Chemical structures of molecules used in this work: anionic monomer NaSS, cationic monomer DMAEA-Q, chemical cross-linker MBAA and UV initiator α-ketoglutaric acid.

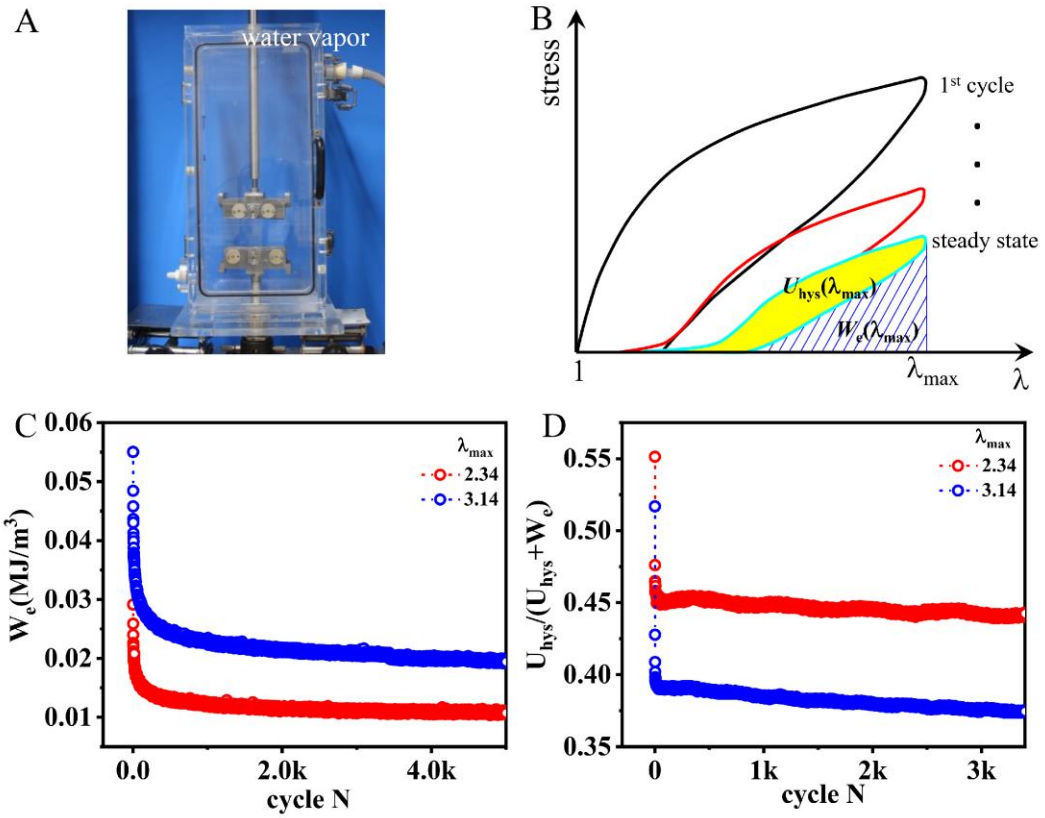

Fig. S2.

Experimental setup for fatigue test and method to obtain energy release rate *G*. (***A***) Photo image of the experimental setup with continuous humidification to prevent hydrogel drying. Before and after the fatigue test, the weight of gel changes less than 2%. (***B***) Scheme of loading-unloading curves to λ_{max} with increasing cycle *N*. The curves drop greatly at the beginning of the cycles and reach a steady state after thousands of cycles. The hysteresis loop shown by the yellow color presents the energy density dissipated during deformation $U_{hys}(\lambda_{max})$, while the area under the unloading curve shown by the blue hatch represent the elastic strain energy density $W_e(\lambda_{max})$. (***C***) Evolution of $W_e(\lambda_{max})$ with cycle *N* for representative samples PA-5 at λ_{max}=2.34 and 3.14, respectively. The $W_e(\lambda_{max})$ drops greatly at the beginning cycles and reaches a steady state after 3000 cycles. $W_e(\lambda_{max})$ at the 3000th cycle is used to estimate the energy release rate *G* by $G=W_e(\lambda_{max})\times H_0$. (***D***) The ratio of $U_{hys}(\lambda_{max})$ to total work of extension $U_{hys}(\lambda_{max})$ + $W_e(\lambda_{max})$ as a function of cycle *N* for PA-5 at λ_{max}=2.34 and 3.14, respectively. It also should be noted that $U_{hys}(\lambda_{max})/(U_{hys}(\lambda_{max}) + W_e(\lambda_{max}))$ for λ_{max}=3.14 is much smaller than for λ_{max}=2.34, indicating that the reassociation ability of ionic bonds decreases at large λ_{max} ($>\lambda_{affine}$).

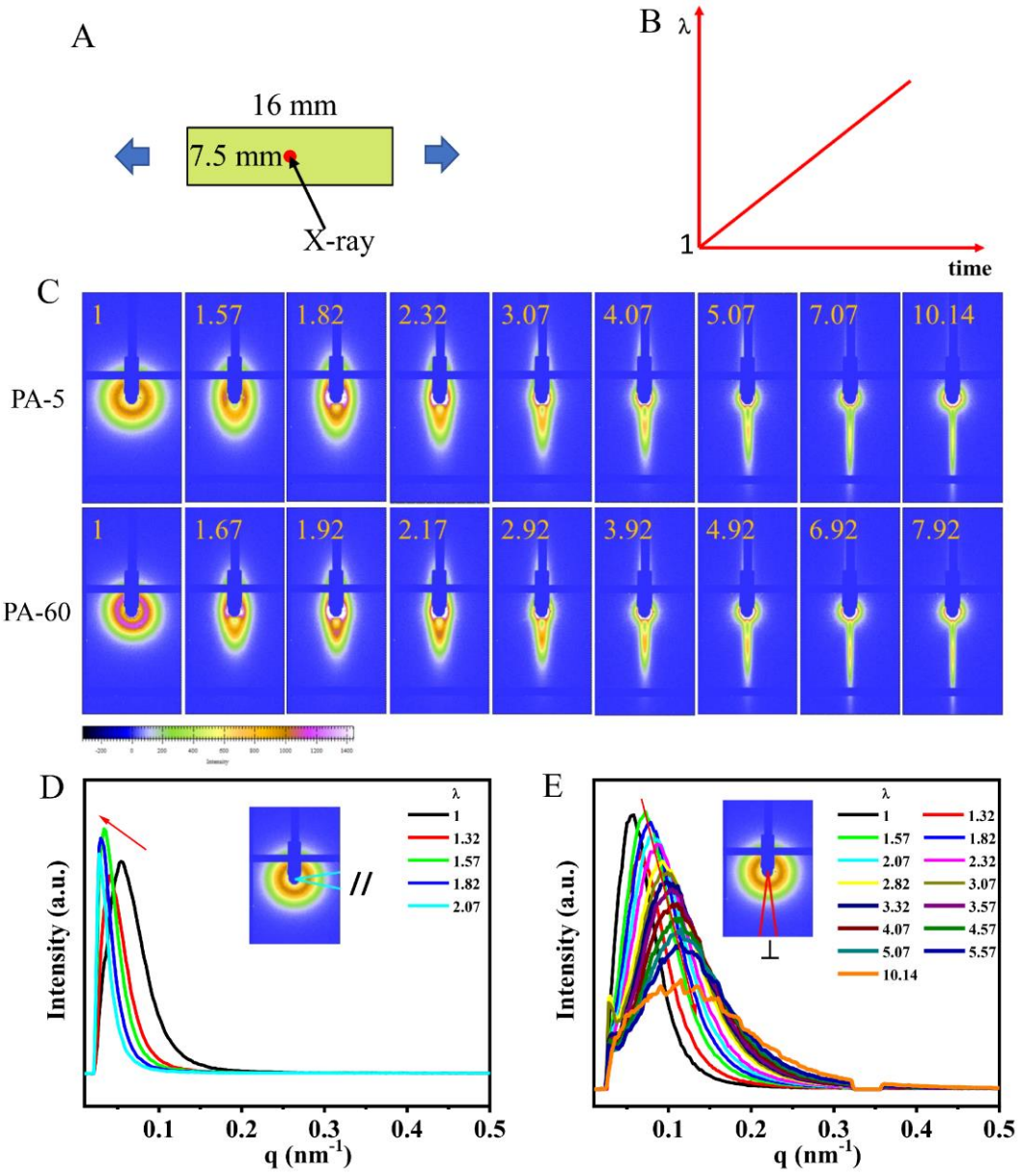

Fig. S3.

In-situ* time-resolved SAXS measurements during tensile test.** (A***) The illustration of the specimen used in *in-situ* SAXS tests. (***B***) Tensile time profile. The nominal strain rate is 1 s^{-1}. (***C***) Evolution of 2D SAXS pattern with λ for representative gels PA-5 and PA-60. (***D*** and ***E***) Evolution of 1D SAXS profiles with λ for PA-5 during tensile tests along the parallel (//) (***D***) and perpendicular (⊥) (***E***) directions. In the parallel direction, the periodic peak shifted to low q with increasing λ and finally beyond the detector range, while the peak shifted to high q in the perpendicular direction. These results demonstrate that the bicontinuous networks are stretched in the tensile direction and compressed in the perpendicular direction. The q at the periodicity peak q_{max} was used to obtain domain spacing (d) by $d=2\pi/q_{max}$.

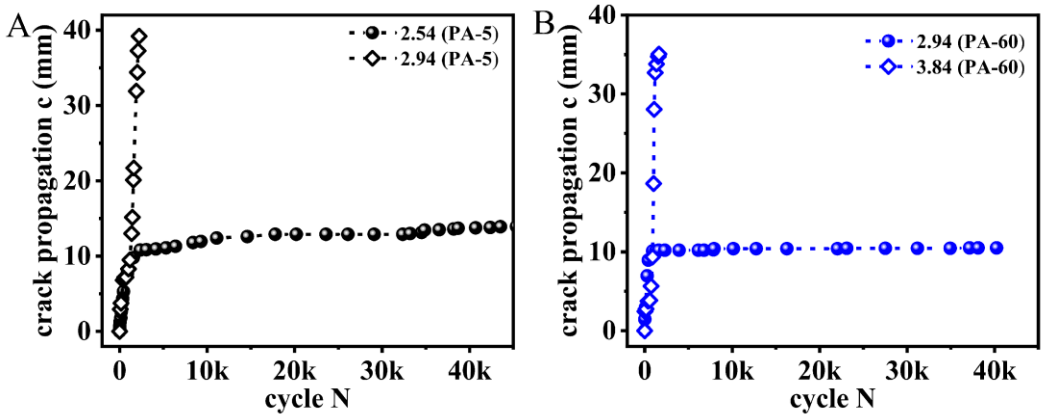

Fig. S4.

Crack propagation length *c* as a function of cycle *N* at representative elongation ratio λ_{max}=2.54 ($<\lambda_{affine}$) and λ_{max}=2.94 ($>\lambda_{affine}$) for PA-5 (***A***), as well as λ_{max}=2.94 ($<\lambda_{affine}$) and λ_{max}=3.84 ($>\lambda_{affine}$) for PA-60 (***B***).

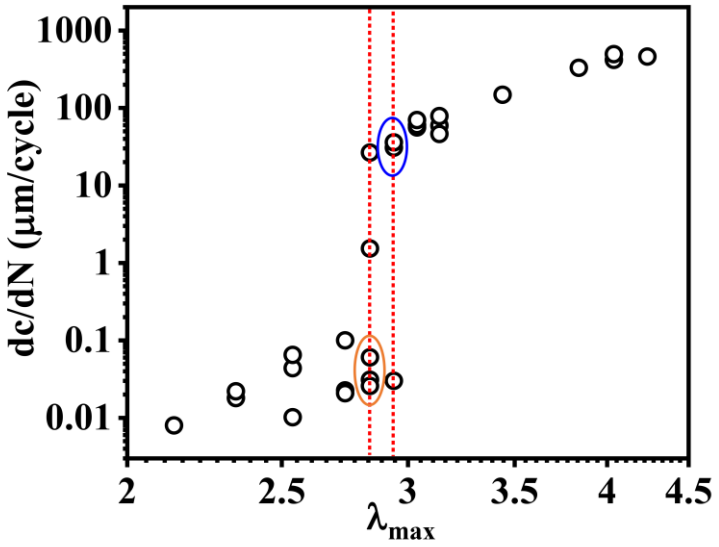

Fig. S5.

The fatigue result for the representative sample PA-5. We observed a narrow transition regime where both slow and fast crack propagation modes co-exist, as shown by the two dotted vertical lines. We determined the λ_{tran} (also G_{tran}) as the middle point in this transition regime (λ_{max}=2.89) and the standard deviation of λ_{tran} (G_{tran}) as the half width of this transition regime. The $\Delta c/\Delta N$ values at the boundary of the transition regime, λ_{max}=2.84 and 2.94 in **Fig. 3** ***D***, ***E***, ***F***, are obtained from the statistical average values of the high probability mode at the corresponding λ_{max}, i.e., the points in orange circle and in blue circle were used to calculate the $\Delta c/\Delta N$ at λ_{max}=2.84 and 2.94, respectively. This method is also applied to sample PA-30 and sample PA-60.

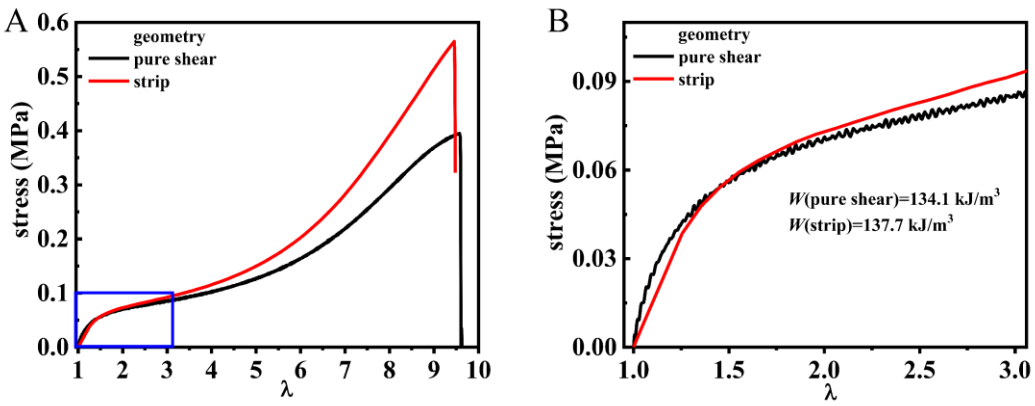

Fig. S6.

Comparison of stress-elongation curves under uniaxial tensile test using sample with the same pure shear geometry in fatigue test (unnotched) and strip geometry in SAXS test. PA-30 is taken as presentative sample. The nominal strain rate is 1 s^{-1}. (***A***) Stress-elongation curves to fracture. The blue rectangle corresponds to the affine deformation regime of hard phase network determined by the SAXS measurement. (***B***) Enlarged affine deformation region. We can see that the differences of stress and work of extension *W* in the affine deformation region between the pure shear geometry and strip geometry are small.

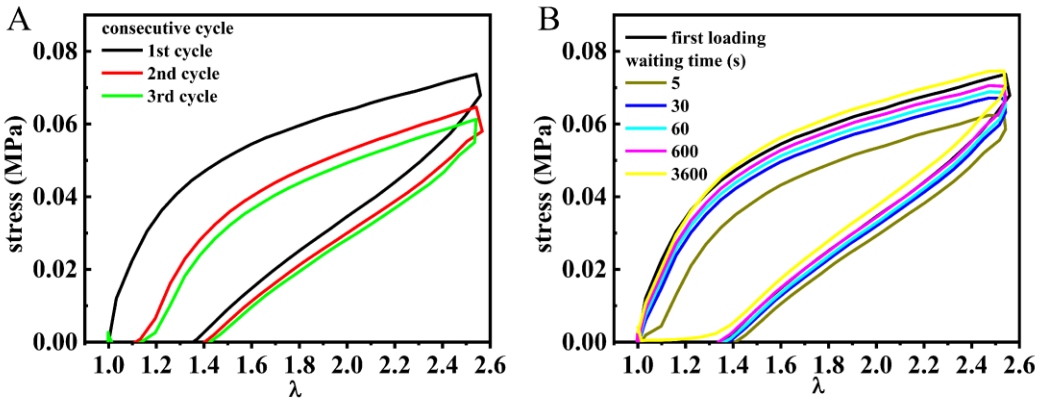

Fig. S7.

Self-recovery behavior of the representative sample PA-30. (***A***) Stress-stretch ratio curves for the sample subjected to consecutive cyclic tensile for 3 cycles under λ_{max}=2.54 with strain rate 1 s^{-1}. (***B***) Loading-unloading curves of the cyclic tensile test at different waiting times between the first consecutive cyclic tensile and reloading. We can see that residual strain exists after consecutive cyclic tensile. The waiting time for sample recovering to its initial length is about 30 s, but it takes more than 600 s for stress-stretch ratio curve recovering completely (recover to the original rearrangement of ionic pairs).

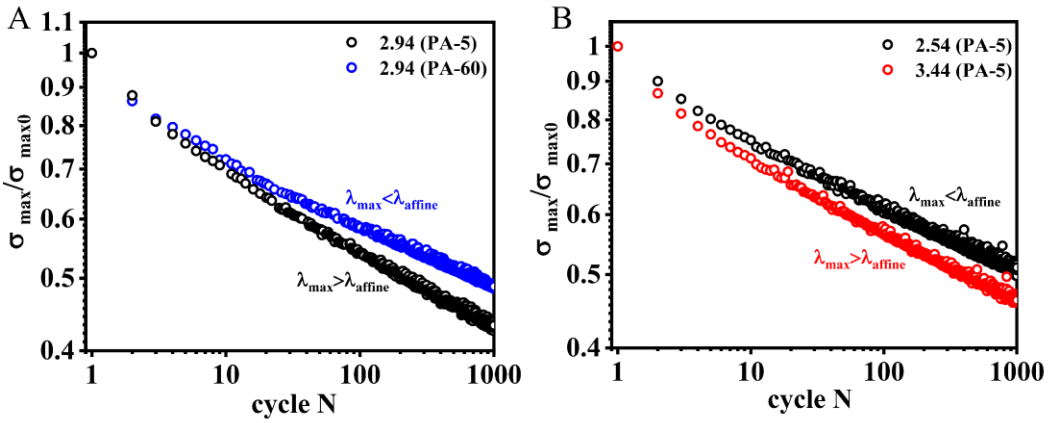

Fig. S8.

Force-carrying ability of unnotched sample under cyclic loading. (***A***) The change of normalized maximum stress ($\sigma_{max}/\sigma_{max0}$) at λ_{max}=2.94 with cycle *N* for samples PA-5 ($\lambda_{max}>\lambda_{affine}$) and PA-60 ($\lambda_{max}<\lambda_{affine}$). (***B***) The change of $\sigma_{max}/\sigma_{max0}$ at λ_{max}=2.54 ($<\lambda_{affine}$) and λ_{max}=3.44 ($>\lambda_{affine}$) with cycle *N* for sample PA-5. The stress carrying ability becomes weaker with cycle *N* for sample experiencing cyclic loading at $\lambda_{max}>\lambda_{affine}$ compared with at $\lambda_{max}<\lambda_{affine}$, owing to the fracture of hard phase network.

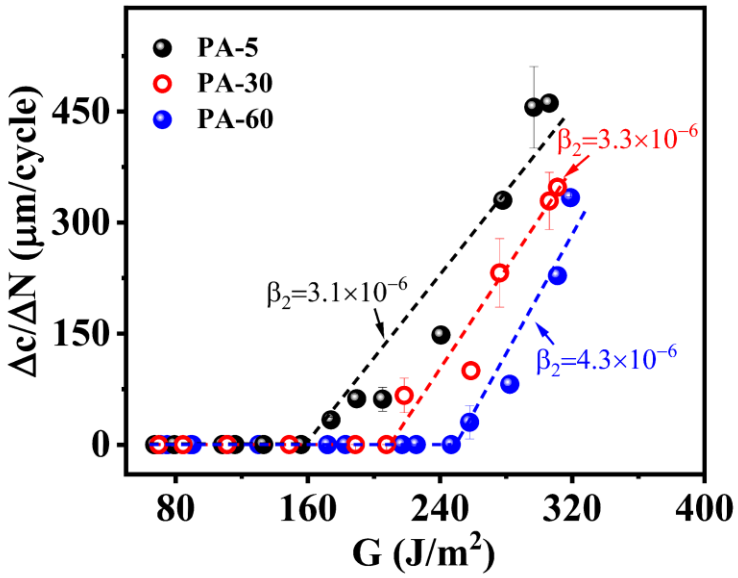

Fig. S9.

Linear plot of Δ*c*/Δ*N* versus *G* in the fast crack propagation regime. Linear relations are observed, and the slope β_2 increases slightly with dialysis temperature of the samples, which is related to the increase of phase contrast of the samples. A higher phase contrast, coming from the larger concentration contrast of the hard and soft phase networks, results in sparser chains in soft phase network, which causes a worse fatigue resistance after fracture of hard phase network.

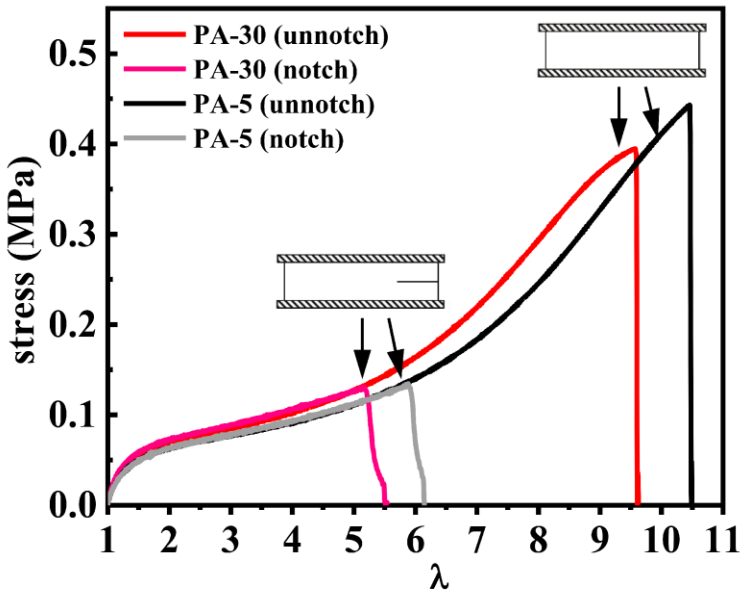

Fig. S10.

Notch sensitivity of PA gels as seen from the tensile behaviors of samples with and without notch in the pure shear geometry. Although the gels without pre-notch can be extended to a large λ (~10), the gels with pre-notch can only be extended to a much smaller λ (5~6). These results indicate that the gels are notch sensitive, due to rupture of the hard phase network at $\lambda > \lambda_{affine}$. The stress is corrected by the initial effective sample width (i.e. L_0=40 mm for notched sample, and L_0=50 mm for unnotched sample).

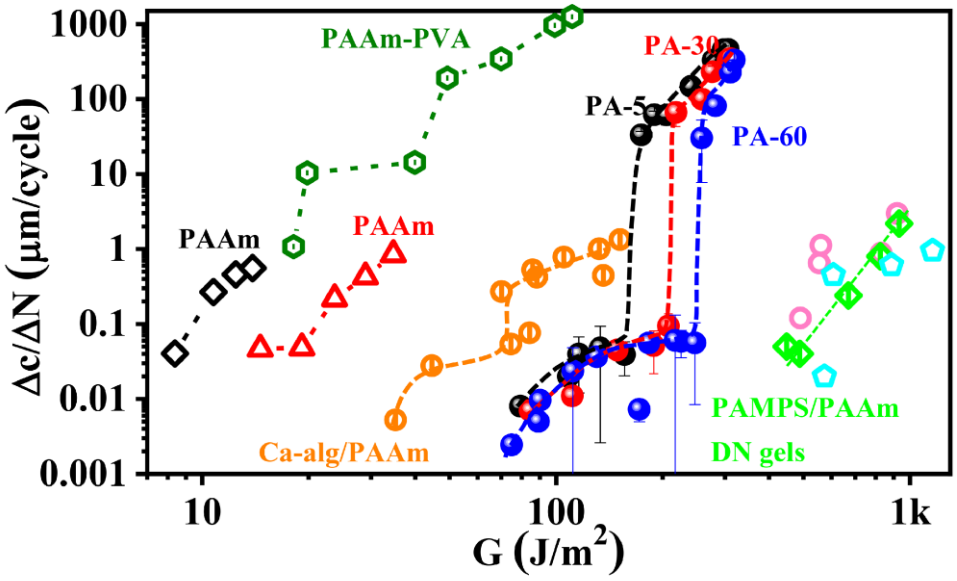

Fig. S11.

Fatigue behaviors of various amorphous hydrogels: elastic single network PAAm gels (the data is collected from the literature (8)), tough PAMPS/PAAm double network (DN) gels(the data is collected from the literature (9)), tough and self-healing PAAm-PVA gels (the data is collected from the literature (10)) and Ca-alginate/PAAm gels (the data is collected from the literature (11)), as well as PA gels studied in this work.

SI References

1. Sun TL, *et al.* (2013) Physical hydrogels composed of polyampholytes demonstrate high toughness and viscoelasticity. *Nat. Mater.* 12(10):932.
2. Ihsan AB, *et al.* (2016) Self-healing behaviors of tough polyampholyte hydrogels. *Macromolecules* 49(11):4245-4252.
3. Ihsan AB, *et al.* (2013) A phase diagram of neutral polyampholyte–from solution to tough hydrogel. *J. Mater. Chem. B* 1(36):4555-4562.
4. Lake G & Thomas A (1967) The strength of highly elastic materials. *Proc. R. Soc. London A* 300(1460):108-119.
5. Creton C (2017) 50th anniversary perspective: Networks and gels: Soft but dynamic and tough. *Macromolecules* 50(21):8297-8316.
6. Rivlin R & Thomas AG (1953) Rupture of rubber. I. Characteristic energy for tearing. *J. Polym. Sci.* 10(3):291-318.
7. Long R & Hui C-Y (2016) Fracture toughness of hydrogels: measurement and interpretation. *Soft Matter* 12(39):8069-8086.
8. Zhang E, Bai R, Morelle XP, & Suo Z (2018) Fatigue fracture of nearly elastic hydrogels. *Soft matter* 14(18):3563-3571.
9. Zhang W, *et al.* (2018) Fatigue of double-network hydrogels. *Eng. Fract. Mech.* 187:74-93.
10. Bai R, Yang J, Morelle XP, Yang C, & Suo Z (2018) Fatigue fracture of self-recovery hydrogels. *ACS Macro Lett.* 7(3):312-317.
11. Zhang W, *et al.* (2018) Fracture toughness and fatigue threshold of tough hydrogels. *ACS Macro Lett.* 8(1):17-23.